Got Coke? Self-Limiting Poisoning Makes an Ultra Stable and Selective Sub-nano Cluster Catalyst

Guangjing Li[1†], Patricia Poths[2†], Tsugunosuke Masubuchi[1], Harry W. T. Morgan[2], Anastassia N. Alexandrova[2‡*], Scott L. Anderson[1‡*]

Affiliations:

[1]Department of Chemistry, University of Utah; 315 S 1400 E, Salt Lake City, UT, 84112, USA

[2]Department of Chemistry and Biochemistry, University of California Los Angeles; 607 Charles E. Young Drive East, Los Angeles, CA 90095, USA

[†]Equal contributions

[‡]Senior authors

[*]Corresponding authors. Email: ana@chem.ucla.edu, anderson@chem.utah.edu

Abstract:

Supported sub-nano clusters hold great promise as economical and highly active catalysts. However, they tend to deactivate rapidly by poisoning and sintering, impeding their widespread use. We find that self-limiting poisoning can stabilize and promote cluster catalysis, i.e., poisoning is not always detrimental, but can sometimes be exploited. Specifically, Pt-Ge alloy clusters supported on alumina undergo slow coking (carbon deposition) under conditions of thermal dehydrogenation, yet preserve strong binding sites. For the case of Pt_4Ge/alumina, theory shows a number of thermally populated isomers, one of which catalyzes carbon deposition. Because the clusters are fluxional at high temperatures, this isomer acts as a gateway, slowly converting all the clusters to Pt_4GeC_2. The surprising result is that Pt_4GeC_2 is highly catalytically active and selective against further coking, i.e., coking produces functional, stable catalytic clusters. Ge and C_2 have synergistic electronic effects, leading to efficient and

25   highly selective catalytic dehydrogenation that stops at alkenes, and improving stability. Thus,

26   under reaction conditions, the clusters develop into a robust catalyst, suggesting an approach to

27   practicable cluster catalysis.

There is a great drive to go sub-nano in precious metal catalysis, because in sub-nano clusters, nearly all the expensive metal atoms are exposed to reactants, increasing cost-effectiveness. Clusters can also have better catalytic activity than the bulk metal[1], provide a parameter for catalyst tuning (size), and can break scaling relations that can limit the activity of larger catalytic centers [2]. Pt-based catalysts are widely used in refining, transforming chemicals, and converting environmentally harmful products [3-7], and the challenge to the use of sub-nano Pt catalysts in such applications relates to stability: deactivation via thermal sintering, and by poisoning. For example, in alkane dehydrogenation for alkene production, sintering may be rapid at operating temperatures, as can poisoning by carbonaceous side products ("coking"). Past research showed that sintering and coking can be inhibited by growing porous overcoatings on nanometer catalyst particles [8], but this approach partially blocks the catalytic sites, limiting efficiency [3,9]. For sub-nano Pt clusters deposited on SiO_2 supports, we showed that even a single layer of overcoating completely blocked all Pt sites, rendering the clusters inert [10]. Another strategy is to periodically regenerate catalysts by oxidizing away carbon deposits at high temperatures, however that would tend to deactivate sub-nano clusters by sintering [11,12]. Alloying sub-nano clusters to modify the chemical and thermal properties is another approach; for example, alloying oxide-supported Pt cluster catalysts with tin or boron prevents carbon deposition and inhibits sintering [13-16], albeit at the cost of losing a substantial fraction of the catalytically active Pt sites.

Germanium was recently suggested by Jimenez-Izal *et al.*[17] as a dopant for small Pt clusters to inhibit coking and sintering under conditions of alkane dehydrogenation. Supported Pt_2Ge clusters were predicted to be more sinter-resistant than Pt_3, Pt_2Sn, and Pt_2Si clusters, and to be highly active for ethane dehydrogenation to ethylene, while resisting deeper dehydrogenation to form coke. Although density functional theory (DFT) simulations were promising, previous

52 experimental work on Ge-containing catalysts was not always successful. For example, several

53 studies found that activity for dehydrogenation of cyclohexane was substantially lower for PtGe

54 catalysts than for analogous Pt catalysts [18,19]. Note, however, that these studies focused on

55 catalysts with particle sizes much larger than the sub-nano clusters examined here. Here we

56 report a novel approach to improving cluster catalyst stability, in which *self-limiting* coking

57 converts the alumina-supported Pt_nGe_x catalyst clusters to a $Pt_nGe_xC_y$ form that is catalytically

58 active and thermally and chemically stable.

59 **Results**

60 **Pt_4Ge/alumina characterization.** As described in the Methods section, Pt_4Ge/alumina

61 samples were prepared by soft-landing mass-selected Pt_4 clusters on thin-film alumina supports,

62 followed by Ge addition by exposure to $GeCl_4$ and H_2. The cluster coverage was 3.8×10^{13}

63 clusters/cm^2, equivalent to 0.1 ML Pt, in the form of Pt_4 clusters. S/TEM imaging on both carbon

64 and alumina-coated aluminum grids is described in the supplementary information (Fig. S1).

65 Individual atoms were not resolved, but from the cluster spot densities, sizes, and stability under

66 the e-beam, we conclude that small Pt_n are stable on both carbon and alumina.

67 X-ray photoelectron spectra (XPS) were used to probe the electronic properties of the

68 Pt_nGe/alumina catalysts and measure the Ge:Pt stoichiometry, which was found to be 1.07:4, i.e.,

69 roughly one Ge atom was deposited *per* Pt_4 cluster. In addition, there was some non-specific Ge

70 deposition on the alumina support, but as shown below and in the supporting information, this

71 alumina-bound Ge is not catalytically active itself, and has little effect on the catalytic properties

72 of Pt_n clusters deposited on a Ge-treated alumina support. As shown in Figure 1, the Ge $2p_{3/2}$

73 peak for Pt_4Ge is shifted slightly to lower binding energy compared to that for Ge bound directly

74 to the alumina support, reflecting the difference in electronic environment.

75

76   **Cluster structures from DFT.** Figure 2 shows the thermally accessible isomers for (Fig.

77   2A) Pt_4/α-Al_2O_3 and (Fig. 2B) Pt_4Ge/α-Al_2O_3 calculated using global optimization at the DFT

78   level, as described in the methods section. The predicted isomer populations at 700 K, near the

79   upper end of the experimental temperature range, are given as P_{700K}. For Pt_4/alumina, the global

80   minimum structure (GM) is a spin-singlet, but all other thermally-accessible local minima (LM)

81   are spin-triplets. The structures have Pt atoms with both positive and negative charges, but in all

82   cases, there is net support-to-cluster electron transfer (ΔQ). For Pt_4Ge/alumina, the GM and all

83   thermally accessible LMs are singlets, with substantial Ge-to-Pt_4 electron transfer, they also all

84   have net support-to-cluster electron transfer.

85   **Ethylene TPD analysis.** For selective alkane dehydrogenation, the desired product is the

86   alkene, and to avoid coking, it is critical that the nascent alkene product desorbs from the

87   catalyst, rather than undergoing further dehydrogenation that ultimately results in carbon

88   deposition. At the same time, it is desirable that the binding energy of the alkene on the catalyst

89   be high because it should lower the barrier for the alkane-to-alkene reaction. To probe the

90   branching between alkene desorption vs. unwanted dehydrogenation/coking, we have adopted

91   the strategy of adsorbing ethylene on the catalyst at low temperature, then measuring, using

92   temperature-programmed desorption (TPD), the branching between desorption of intact ethylene,

93   vs. hydrogen desorption, which signals dehydrogenation and carbon deposition. To directly

94   examine the propensity toward carbon deposition, we have also measured the C 1s XPS

95   intensities after multiple ethylene adsorption/desorption cycles.

96   Figure 3 shows TPD data collected for Pt_4/alumina and Pt_4Ge/alumina samples, both with

97   identical, 0.1 ML-equivalent of Pt deposited as Pt_4 clusters. The data shown are from

98   experiments in which 21 sequential TPD runs were done for each sample. For each run, the

99   sample was first exposed to a saturation dose of C_2D_4 (10 L) at 150 K, and then heated at 3 K/sec

100   to 750 K while mass-spectrometrically monitoring desorption of C_2D_4 and D_2. No signal was

101   observed for desorption of acetylene or other hydrocarbon species, and no additional D_2

102   desorbed in test experiments in which the samples were ramped to higher temperatures,

103   indicating that ethylene either desorbed intact, or dehydrogenated to $2\ C_{(ads)} + 2\ D_{2(gas)}$.

104   For comparison, the figure also shows the desorption signals observed from the alumina and

105   Ge-treated alumina (Ge/alumina) supports with no Pt/PtGe clusters. For both supports, C_2D_4

106   corresponding to a few percent of a monolayer adsorbed during the 150 K dose, desorbing below

107   250 K when heated. This support-bound C_2D_4 might be bound at defects in the alumina film, for

108   example. No D_2 desorption was observed, showing that neither the alumina nor Ge/alumina

109   supports were active for ethylene dehydrogenation, and as might be expected, the desorption

110   signals in repeated runs were unchanged.

111   During the 1st TPD from the Pt_4/alumina sample, there was substantial C_2D_4 desorption in

112   the 250 – 450 K range, corresponding to ethylene binding to the Pt_4 clusters, in addition to a

113   lower temperature feature attributed primarily to weak binding to the alumina support. D_2

114   desorbed in a broad feature extending from 250 K to 750 K, implying that many of the C_2D_4

115   molecules dehydrogenated, liberating D_2 and depositing carbon. During the 2nd run there was

116   substantially less C_2D_4 desorption above 250 K and a general shift to desorption at lower

117   temperatures, implying fewer and weaker C_2D_4 binding sites. The amount of D_2 desorption also

118   decreased, suggesting that dehydrogenation occurs primarily for strongly bound C_2D_4, but the

119   number of such sites was much smaller in the 2nd TPD cycle. As additional cycles were carried

120   out, the decrease in C_2D_4 desorption at high temperatures, and the reduction in D_2 desorption

121   continued, with the rate of change slowing as the clusters were mostly deactivated.

122   The 21 TPD run experiments took >20 hours each, making repetition impractical and raising

123   the possibility that surface contamination might have influenced the results in later cycles.

124   Therefore, we also carried out repeated experiments studying the effects of the first six TPD

125   runs, which, indeed, were responsible for most of the change in catalyst properties. Quantitative

126   analysis of the desorption is based on these six-TPD experiments. As described elsewhere[13] it is

127   possible to calibrate the absolute sensitivity of the TPD system, and Table S1 gives the numbers

128   of C_2D_4 and D_2 molecules desorbing *per* Pt_4 cluster in each of the 6 TPD runs, averaged over the

129   four available data sets. Because there was no evidence of adsorbed hydrogen remaining at 750

130   K, the number of C atoms deposited should be equal to the number of D_2 molecules desorbing,

131   and the total number C_2D_4 molecules adsorbed during each 150 K dose can be estimated as the

132   number C_2D_4 desorbing + half the number of D_2 desorbing. During the 1st TPD, an average of

133   ~2.9 C_2D_4/Pt_4 were adsorbed, of which ~56% desorbed intact, with the remainder

134   dehydrogenating to liberate D_2 and deposited an average of ~2.5 C atoms/cluster. Because of the

135   cluster isomer distribution, some cluster-to-cluster variation is expected, but we interpret the 1st

136   TPD desorption numbers as indication that three C_2D_4 molecules typically adsorbed per cluster

137   at 150 K, two of which typically desorbed intact upon heating, the other one decomposed to

138   liberate 2 D_2(gas) and deposited 2 C per cluster, on average. By the 6th TPD cycle, the number

139   of C_2D_4 adsorbed *per* Pt_4 had dropped ~58% to just ~1.23, of which ~82% desorbed intact, with

140   the remainder decomposing to deposit C and liberate D_2. For the Pt_4/alumina sample, the total

141   D_2 desorption during the 6 TPD runs corresponded to the deposition of ~5.75 C atoms *per*

142   deposited Pt_4 cluster.

143   Pt_4Ge/alumina presents a striking contrast. As described in the Methods, the final step in

144   Pt_4Ge/alumina preparation involved 750 K heating to desorb residual Cl and hydrogen (as HCl

145   and H_2 – Fig. S2), and to emphasize the point that the Pt_4Ge/alumina samples had already been

146   heated once prior to the initial C_2D_4 TPD runs, the TPD cycles in Fig. 3 D and E are numbered

147   starting with "2nd TPD". The C_2D_4 desorption observed in this 2nd TPD for Pt_4Ge/alumina was

148   quite similar in both intensity and structure to that in the 1st run on Pt_4/alumina, with a low-

149   temperature component at least partly due to desorption from the Ge/alumina substrate, and a

150   high-temperature component attributed to sites on the Pt_4Ge clusters. In contrast, D_2 desorption

151   (i.e., carbon deposition) was much weaker for Pt_4Ge than in either the 1st or 2nd TPD runs for

152   Pt_4/alumina, and had a bi-modal temperature dependence, suggesting that what little D_2

153   desorbed, was produced by two processes with different activation energies. The D_2 desorption

154   features can, in principle, be fit to extract E_a values, requiring some assumption about the kinetic

155   order of the rate-limiting step. We previously examined D_2 TPD from small Pt_n/alumina under

156   conditions similar to those here[20], observing recombinative desorption starting at ~230 K,

157   peaking just below 300 K, and terminating at ~450 K. The fact that the desorption features for

158   D_2 generated by C_2D_4 decomposition do not match the recombinative feature observed in

159   D_2 TPD, suggests that some other step in the D_2 production pathway is rate-limiting. For

160   simplicity, we assume that this step follows 1st order kinetics[21], and further assume a prefactor of

161   10^{15} sec^{-1}. This crude approximation gives effective (or averaged over multiple accessible

162   pathways) E_a values of ~1.1 V for the 350 K feature, and ~2.5 eV for the 500 K feature, in the

163   range observed for C-H activation in the DFT calculations. During subsequent TPD cycles, there

164   continued to be a small and reducing amount of D_2 production, and the C_2D_4 desorption behavior

165   evolved, but note that when a steady state had been reached after ~15 runs, the C_2D_4 desorption,

166   particularly at higher temperatures, was substantially higher for Pt_4Ge than for Pt_4.

167   Again, quantitative desorption analysis was done for the first 6 TPD where multiple

168   experiments were available. The total number of C_2D_4 molecules adsorbed *per* Pt_4Ge cluster in

169   the 2nd TPD was ~1.71, of which ~86% desorbed intact, with the balance decomposing to

170   liberate D_2 and deposit ~0.5 C/cluster on average (Table S2). Given that C atoms deposit in

171   pairs, we interpret this to mean that the Pt_4Ge clusters initially had one or two C_2D_4 molecules

172   adsorbed, and that on ~25% of the clusters, one ethylene decomposed to deposit two C atoms.

173   Thus, the probability of carbon deposition during this 1st TPD run was ~one-fourth that for the

174   Pt_4/alumina samples. By the 6th TPD cycle, the number adsorbing C_2D_4 molecules was still

175   ~1.46/cluster, of which 91% desorbed intact, with the balance decomposing to liberate D_2 and

176   deposit just ~0.28 C/Pt_4Ge cluster. Thus, during the 2nd TPD for Pt_4Ge/alumina, the number of

177   ethylene adsorbing *per* cluster was ~41% *lower* than in the 1st TPD for Pt_4/alumina, but by the 6th

178   TPD, the number was ~20% *higher* for Pt_4Ge. We interpret this to imply that addition of a Ge

179   atom reduced the initial number of ethylene binding sites, but the binding sites, and particularly

180   the catalytically important strong/high temperature binding sites, survived much better under

181   reaction conditions for Pt_4Ge than for Pt_4.

182   From the total D_2 desorption during the 6 TPD runs, we estimate that the total carbon

183   deposition on Pt_4Ge/alumina amounts to ~1.8 C atoms *per* deposited Pt_4Ge cluster, which is less

184   than a third the total estimated for Pt_4/alumina (5.75 C/cluster). It should be noted that due to

185   uncertainties in the intensity calibration process, the absolute desorption numbers given here and

186   in Tables S1 and S2 are uncertain by ~50%, however, the relative uncertainties for comparing

187   TPD data in different experiments are smaller – on the order of ±10%. Thus, the TPD data

188   indicate that Pt_4/alumina cokes more than a factor of three faster than Pt_4Ge/alumina.

189   **Carbon deposition analysis.** Carbon deposition was also probed directly by C 1s XPS after the

190   6 TPDs, as summarized in Figs. 3C and 3F. Also shown are the C 1s XP spectra measured for Pt-

191   free alumina and Ge/alumina samples after 6 C_2D_4 TPD. The signals are weak because the

192   coverage of clusters, responsible for most carbon deposition, was small, as is the C 1s

193   photoemission cross section. Nonetheless, it is clear that the C 1s signal for Pt_4/alumina is

194   substantially larger than the signal for the alumina support, and after subtracting the support

195   contribution, the net carbon deposition corresponds to ~8 ± 5 C atoms/cluster. The C/Pt ratio

196   was calculated assuming both C and Pt are in the surface layer, in which case C/Pt =

197    $(I_C \cdot \sigma_{Pt})/(I_{Pt} \cdot \sigma_C)$, where I_C and I_{Pt} are the integrated intensities for the C 1s and Pt 4d peaks, and σ_C

198   and σ_{Pt} are the sublevel photoemission cross sections[22]. The C 1s signal for the Pt_4Ge/alumina

199   sample is smaller, and after subtracting the support contribution, the carbon deposition is

200   estimated to be 3 ± 3 C atoms/Pt_4Ge cluster. Thus, both the absolute number of deposited

201   C atoms/cluster, and the ~3:1 ratio of C deposition on Pt_4 compared to Pt_4Ge, are consistent with

202   the values derived from analysis of D_2 TPD.

203   To provide additional insight into the carbon/Pt morphology, the samples were also probed

204   by low energy He^+ ion scattering (ISS) before and after 6 TPDs (Fig. 4). Example ISS spectra

205   shown as insets have peaks due to He^+ scattering from individual Pt, Ge, Al, and O atoms in the

206   top-most sample layer, superimposed on a smooth background from multiple or sub-surface

207   scattering processes. The background rises sharply at lower energies, preventing direct

208   observation of surface carbon. The main plots in Fig. 4 show how the background-subtracted Pt

209   and Ge peak intensities vary as a function of exposure to the ~0.35 μA He^+ beam, which slowly

210   sputters materials from the surface. To compensate for any He^+ intensity variations, the Pt and

211   Ge intensities are normalized to the total (Pt+Ge+Al+O) intensity, which is nearly invariant

212   under He^+ exposure.

213   For as-deposited Pt_4/alumina (Fig. 4A), the Pt ISS intensity initially increased slightly, then

214   slowly declined at long exposures as Pt atoms were slowly sputtered from the surface. The slight

215   increase was attributed to exposure of additional Pt due to sputter removal of a small coverage of

216   adventitious adsorbates, e.g. H_2 or CO, which have partial pressures $\leq$ ~5 x 10^{-11} Torr in the

217   UHV system. If an as-deposited Pt_4/alumina sample is briefly heated to 750 K to remove the

218   adsorbates prior to ISS analysis (Fig. 4B), the Pt intensity is substantially higher than in the

219   unheated sample, and simply decreases with exposure time as Pt is sputtered. Note that if the Pt_4

220   clusters had sintered at 750K to form larger, multilayer clusters on the surface, this would have

221   substantially *decreased* the Pt ISS intensity, thus such extensive sintering is ruled out by the

222   result in Fig. 4B, consistent with the conclusions from the TEM data. The initial Pt ISS intensity

223   for Pt_4/alumina after a single C_2D_4 TPD experiment (Fig. 4C) was ~18% smaller than that for the

224   750 K heated Pt_4/alumina sample in Fig. 4B, suggesting some attenuation of Pt signal by

225   deposited carbon, and the attenuation increased after 6 TPDs (Fig. 4D), as expected.

226   The as-prepared Pt_4Ge/alumina sample was probed both before (Fig. 4E) and after (Fig. 4F)

227   the 750 K heating used to remove residual H and Cl from clusters. For the unheated clusters, the

228   initial Pt and Ge intensities were small, increasing as the adsorbed H and Cl were sputtered,

229   exposing underlying Pt and Ge atoms, and then decreasing slightly at long exposures as Pt and

230   Ge were lost to sputtering. For the sample probed after 750 K heating (Fig. 4F), the initial Pt and

231   Ge intensities were similar to the maximum intensities seen for the unheated sample, i.e.,

232   removing the adsorbates by heating vs. He^+ sputtering had similar effects. The initial Pt ISS

233   signal for the heated Pt_4Ge/alumina sample was ~37% smaller than the signal observed for

234   heated Pt_4/alumina, presumably reflecting some shadowing or blocking of He^+ scattering from Pt

235   by the Ge atom. The 37% lower Pt ISS intensity was quite similar to the 41% lower total

236   adsorbed C_2D_4 measured in the initial Pt_4Ge/alumina TPD (Tables S1 and S2). For

237   Pt_4Ge/alumina samples that were heated to 750 K then subjected to 1 or 6 TPD runs (Fig. 4G and

238   H), the Pt intensities were attenuated compared to the heated sample, as expected from the fact

239   that some carbon deposition occurred.

240   The post-6-TPD initial Pt ISS intensity for the Pt_4/alumina sample (Fig. 4D) was ~44%

241   attenuated, compared to the initial intensity of the 750 K heated Pt_4/alumina sample. It is not

242   surprising that there was attenuation, given the carbon deposition observed by TPD and XPS (~6

243   C/cluster from TPD, ~8 C/cluster from XPS). Indeed, the surprise is that the attenuation was not

244   much larger. For example, 5- and 20-fold attenuations of the Pt ISS signals were found to result

245   from adsorption of just a single layer of H or O atoms, respectively, on sub-nano Pt_n/SiO_2[23].

246   Thus, the much smaller Pt ISS attenuation indicates that the C atoms must be bound in sites

247   where they have little effect on He^+ scattering from Pt – such as cluster periphery or buried in the

248   cluster core. For the Pt_4Ge/alumina sample after 6 TPDs (Fig. 4H), the initial Pt signal was

249   ~31% attenuated, relative to the heated Pt_4Ge/alumina (Fig. 4F), which can be compared to the

250   amount of C deposition seen from TPD (~1.8/cluster) and XPS (~3/cluster). For both Pt_4 and

251   Pt_4Ge samples, ISS indicates that a significant fraction of the Pt atoms remained accessible to

252   He^+ scattering after 6 TPD runs.

253   To summarize the experiments, adding a single Ge atom reduces carbon deposition by a

254   factor of ~three, but there is still significant carbon deposition for Pt_4Ge, amounting to two or

255   three C atoms/cluster after 6 TPD runs. Nonetheless, the Pt_4Ge clusters retain most of their

256   strong/high temperature ethylene binding sites, even after 21 TPD runs, while these the high

257   temperature sites are almost entirely suppressed for Pt_4/alumina. Questions we seek to address

258   are: Why is carbon deposition only partly suppressed for Pt_4Ge/alumina? What is the nature of

259   the strong (high temperature) ethylene binding sites retained for Pt_4Ge but lost for Pt_4/alumina?

260   And why, despite retaining strong C_2D_4 binding sites, does Pt_4Ge clusters nearly stop producing

261   D_2? DFT was used to address these questions and also to examine the activity of the model

262   catalysts for the ethane-to-ethylene dehydrogenation reaction, which cannot be studied under

263   surface science conditions.

264   **DFT of ethane, ethylene, and acetylene C-H activation barriers.** Pt_4Ge/alumina clusters

265   are found to strongly bind and activate ethane on all thermally accessible isomers (Fig. 2B), and

266   there are well over 50 configurations for C_2H_6-Pt_4Ge/alumina with energies below 0.4 eV, i.e.,

267   with non-zero thermal populations at 700 K. All of the low-lying configurations appear to

activate ethane, as shown by C-H bond elongations ranging from 1.140 Å to 1.158 Å, compared

to the un-activated C-H bond length of 1.09 Å. Figure 5A illustrates two reactant configurations

and gives energies (horizontal lines) for a dozen more. The two illustrated are built on the GM

and on the second local minimum (LM2) for the bare Pt_4Ge cluster. The LM2-based structures

are singled out for reasons that will be made clear shortly. Once adsorbates bind to LM2, the

structures are labeled LM', because their thermal accessibility is changed by the binding of

adsorbates. For all the lowest-energy configurations, the activation barriers for breaking the first

C-H bond are found to be ≤ 0.4 eV, well below the energy for desorption of ethane from the

clusters (≤ 0.6 eV, see Fig. S3 and text). Thus, DFT shows that ethane should bind to all isomers

of Pt_4Ge/alumina, and dehydrogenate in preference to desorbing. Another factor that tends to

promote dehydrogenation is that the H atom products readily recombine and desorb as H_2 at

moderate temperatures, as shown in Fig. 3E.

   To examine the pathways that must ultimately lead to carbon deposition, we next performed

DFT calculations of ethylene and acetylene binding and dehydrogenation on the thermally-

accessible isomers of the Pt_4Ge clusters (Figs. 5B and 5C). Note that adsorbates can bind with

different energies on different cluster isomers, which can significantly change isomer

populations, with important effects on the mechanism. We found that ethylene predominantly

binds to the Pt_4Ge clusters (including the most abundant GM) in the π-mode, i.e. with the

ethylene π bond coordinated to a single Pt atom, retaining the C sp^2-hybridization. The barriers

for such π-mode-bound ethylene to undergo C-H dissociation are higher than the desorption

energies, and thus π-mode-bound ethylene is predicted to mostly desorb intact, rather than

undergoing further dehydrogenation, consistent with the small D_2 desorption branching observed

for the Pt_4Ge/alumina catalyst. Importantly, however, one of the thermally-accessible isomers of

ethylene-Pt_4Ge, LM' (corresponding to LM2 of the bare cluster), binds ethylene in a di-σ mode

(Fig. 5B), and in this configuration the barrier to C-H dissociation is significantly lower than in any of the π-mode-bound configurations. LM2 for the bare cluster has P_{700K} of only 0.3% – far too small to account for the amount of D_2 desorption observed during TPD. However, the ethylene di-σ bond in LM' is strong, stabilizing LM' and increasing its P_{700K} to ~3%.

We propose that dehydrogenation on an isomer with small, but significant population, accounts for carbon deposition being only partly suppressed for Pt_4Ge/alumina. Specifically, during each TPD cycle, most of the Pt_4Ge would desorb C_2D_4 intact, but the small fraction in LM' configurations would dehydrogenate C_2D_4, giving rise to the observed small D_2 signals. Isomerization between the thermally accessible isomers within the ensemble ensures that LM' is re-populated each TPD cycle, thus LM' acts as a "gateway" isomer that keeps dehydrogenating ethylene on a fraction of the cluster population during repeated TPD cycling. We expect that all of the clusters eventually pass through this gateway during repeated TPD cycling, and become coked. The calculated population of the C_2D_4-LM' isomer (~3%) is smaller than the population (~25%) suggested by D_2 TPD signal, however, we note that isomer populations depend exponentially on their energies, thus amplifying the effects of small DFT errors.

For coke to form, dehydrogenation must proceed further, beyond acetylene. With acetylene bound to Pt_4Ge (Fig. 5C), the isomer populations adjust again: the LM' isomer drops even further in energy relative to the GM, such that its P_{700K} increases to ~10% of the total population. The population dehydrogenates acetylene with a high propensity, rather than desorbing it, as suggested by the fact that in a number of the low-lying isomers of C_2H_2-Pt_4Ge/alumina, acetylene dehydrogenates spontaneously (Fig. S5). For the thermally accessible isomers in which C_2H_2 remains intact, the computed first C-H dissociation barriers are well below the desorption energies for intact acetylene, which exceed 2 eV from all isomers (Fig. 5C). Notably, LM'-based isomers continue to dehydrogenate more aggressively than GM-based isomers,

316   judging by the computed barriers, and new Pt_4Ge core isomers are stabilized due to the strong

317   binding of acetylene, provide lower-barrier routes for dehydrogenation (Fig. 5C, dashed lines).

318   Hence, theory predicts that once acetylene forms on the Pt_4Ge cluster, regardless of the isomer, it

319   will always dehydrogenate, though higher-energy isomers will dehydrogenate at lower

320   temperatures, some with dehydrogenation barriers less than 1 eV. This prediction is consistent

321   with the observation that no intact acetylene desorption is ever seen for Pt_4Ge/alumina in the

322   experiments (Fig. S6). Thus, in ethylene TPD (and in the ethane-to-ethylene reaction), we

323   predict that Ge addition largely, but not completely, suppresses carbon deposition, such that in

324   repeated TPD cycles (or long reaction times) the clusters will slowly all become coked by at least

325   a pair of carbon atoms, with the LM' isomer serving as a gateway to coking.

326   To assess the favorability of dehydrogenation versus C-C bond breaking (cracking), we

327   computed the energetics (and barriers) of cracking compared to C-H activation. For the Pt_4Ge

328   cluster, we found no cracking pathways that could compete with C-H activation either

329   thermodynamically or kinetically. The single structure that might compete is shown in Fig. S4,

330   however, but it is both thermodynamically more uphill than any C-H activated endpoints and has

331   a higher barrier than any of the LM' dehydrogenation barriers.

332   The next question posed by the experiments is how Pt_4Ge/alumina retains its high-

333   temperature ethylene binding sites after 21 TPDs, even though the C 1s XPS and ISS results

334   indicated significant carbon deposition. The DFT results indicate that once dehydrogenation has

335   gone beyond ethylene, it should proceed to completion, depositing a pair of C atoms. Therefore,

336   we study the Pt_4GeC_2/alumina system with DFT, finding, surprisingly, that only a single Pt_4GeC_2

337   isomer was thermally accessible (Fig. 6A). This structure is recognizably a relative of LM' that

338   has incorporated two carbon atoms as an intact C_2 unit into the middle of the cluster, maximizing

339   the number of Pt-C bonds. Theory thus predicts that all the Pt_4Ge clusters will eventually reach

this single Pt_4GeC_2 structure as they coke via the LM' gateway isomer. Because the carbon is located in the center of the Pt_4 ring, it does not physically block any Pt sites, in agreement with the observed minimal Pt ISS attenuation.

The presence of C_2 does, however, alter the electronic structure of the cluster, apparently stabilizing the system, as it collapses the Pt_4Ge isomer distribution to just the one structure in Fig. 6A – a thermodynamic sink. The C_2 unit acts as an oxidant, developing a net negative charge of -0.42 e, while the Ge atom has a +0.80 e positive charge, i.e. it loses further electron density compared to Ge in Pt_4Ge. The overall charge on the Pt_4 moiety remains negative, decreased slightly from the values typical for Pt_4Ge isomers, but is still higher than that for Pt_4/alumina (Figs. 2A and 6A). The interaction of C_2 with Pt_4Ge is strikingly different from its interaction with Pt_4, as shown in Fig. S7. To investigate the electronic structure differences between the Pt_4C_2 and Pt_4GeC_2 clusters in more detail we calculated the molecular orbitals (MOs) of unsupported anionic gas-phase models in which the coordinates of all atoms were held fixed at values determined for the supported clusters (Fig. S8 A and B). These minimal models are validated by their Bader charge distributions, which show the same trends as their supported counterparts[24,25]. The MO diagrams (Fig. S8C) show that the Ge atom in Pt_4GeC_2 is in the +2 oxidation state; the first three unoccupied MOs are all Ge-Pt antibonding combinations with predominant Ge $4p$ character, while the Ge $4s$-based MO is found far below the HOMO in energy. Of further interest is the LUMO of Pt_4C_2, which corresponds to the HOMO in Pt_4GeC_2 after accepting an electron pair from Ge. This orbital has clear C-C π bonding character, so the effect of adding Ge to Pt_4C_2 is to strengthen the C-C bonding in the partially coked cluster.

While Pt_4C_2 and Pt_4GeC_2 are structurally similar, have similar total amounts of electron transfer from the support, and feature the partially negatively charged C_2 unit, they differ in the source of electron transfer to C_2: In Pt_4GeC_2, C_2 receives electrons largely from Ge, leaving Pt

364 still quite anionic. In Pt_4C_2, C_2 draws electrons from Pt, leaving it closer to the charge neutral

365 state. Thus, it appears that in Pt_4Ge/alumina, Ge and C_2 are in a synergistic electronic

366 relationship that preserves the net negative charge on the Pt_4 moiety. Hence, Pt sites are neither

367 blocked nor significantly changed electronically in Pt_4GeC_2/alumina as compared to Pt_4Ge, and

368 therefore, it is not surprising that Pt_4GeC_2 retains the C_2D_4 binding properties seen in the TPD.

369 Hence, we expect Pt_4GeC_2/alumina to exhibit the catalytic activity and selectivity comparable to

370 those of Pt_4Ge/alumina.

371   The important remaining questions are whether Pt_4GeC_2/alumina is still active for ethane-to-

372 ethylene dehydrogenation, and whether it is selective against additional carbon deposition,

373 thereby resisting deactivation. Ethane dehydrogenation on Pt_4GeC_2 is addressed in Fig. 6B.

374 Binding of ethane and ethylene on the Pt_4GeC_2 cluster in various geometries was sampled (Figs.

375 S9 and S10), and then the barriers for C-H dissociation calculated. We again found that the

376 barriers to ethane C-H activation were generally lower than the desorption energies for ethane

377 from the cluster, suggesting that the Pt_4GeC_2 cluster should still be highly active for ethane to

378 ethylene dehydrogenation. To be stable with respect to further carbon deposition, it is necessary

379 that the resulting ethylene desorb instead of dehydrogenating further. For ethylene on

380 Pt_4GeC_2/alumina (Figs. S10 and 6C), some configurations were calculated to have highly

381 endothermic (>1.2 eV) dehydrogenation, and in others, the activation barriers were high (>2 eV).

382 Some structures showed the possibility for dehydrogenation of ethylene, with barriers between

383 1.3-1.5 eV to access structures that are not highly endothermic, however, we note that these

384 barriers are higher than those for the dehydrogenation of ethylene on the Pt_4Ge cluster, indicating

385 that the Pt_4GeC_2 cluster is even more selective than the initial Pt_4Ge catalyst. Acetylene

386 dehydrogenation by Pt_4GeC_2 (Fig 6D) either retains very high barriers (>2 eV), or has such low

387 barriers for the reverse reaction of re-hydrogenation that dehydrogenation remains unlikely. We

388   note that there is only one thermally accessible acetylene binding mode (Fig 6D, left-most inset),

389   which involves the binding of acetylene to two Pt atoms, in a mixed π-/σ-fashion, as well as

390   binding to a C in the C_2 unit. This collapse of accessible modes is reminiscent of that of Pt_4Ge to

391   Pt_4GeC_2, which is likewise likely attributable to the formation of multiple Pt-C bonds, as well as

392   an additional C-C bond. It is therefore possible that the cluster cokes further, albeit at an even

393   slower rate once coke has begun to form, based on the heights of C-H activation barriers for

394   ethylene and acetylene on the Pt_4GeC_2 cluster.

395   In order to assess possible coke formation via cracking on Pt_4GeC_2, we also computed the

396   energetics of the C-C bond scission on relevant intermediates. A few of the pathways found are

397   thermodynamically viable, however the kinetics render them unlikely compared to either C-H

398   activation or desorption (Fig. S11), with the exception of acetylene cracking, where the barrier

399   remains ~ 0.3 eV higher than the lowest barrier for C-H activation.

400   Ultimately, however, DFT calculations suggest that while coke formation on the Pt_4Ge

401   system is not avoided, the cluster nonetheless retains its active and selective nature towards

402   alkane dehydrogenation. Thus, the conclusion is that selectively-coked Pt_4GeC_2/alumina,

403   generated under reaction conditions by a self-limiting coking process, is the actual stable, active,

404   and selective catalyst for alkane-to-alkene dehydrogenation.

405   **Conclusion**

406   In summary, from the TPD, XPS, and DFT results, we found that Pt_4Ge/alumina promotes

407   intact desorption of ethylene in ethane dehydrogenation, largely, but not completely preventing

408   carbon deposition. There is one minority isomer of Pt_4Ge/alumina (LM2, or LM') that acts as a

409   gateway to carbon deposition on Pt_4Ge/alumina, gradually resulting in all the Pt_4Ge clusters

410   becoming coked. However, defying expectations, coking is not detrimental to catalytic activity,

411   and instead preserves the desired catalytic properties while dramatically enhancing cluster

412   catalyst stability. The coking is self-limiting: once Pt_4GeC_2/alumina forms, it dramatically

413   decreases the further deposition of carbon by ethylene dehydrogenation via increased barriers for

414   ethylene desorption, eventually reaching a steady-state catalyst where no further changes in the

415   ethylene binding sites or D_2 desorption are observed experimentally. Furthermore,

416   Pt_4GeC_2/alumina still binds ethane strongly, with low activation barriers for ethane-to-ethylene

417   conversion. Thus, the self-limiting coking of Pt_4Ge improves the selectivity of the catalyst

418   without degrading the activity. The Ge atom in the cluster interacts with the carbon in the coked

419   cluster, stabilizing the cluster significantly, and prevents deactivation of the cluster via either

420   physical blocking of sites, or dramatic change in electronic structure. This moderates the

421   tendency of the cluster to coke, enabling the self-limiting behavior. The synergy between

422   alloying and selective coking could be a way forward in creating ultra-stable sub-nano cluster

423   catalysts for other reactions, solving the main limiting factor hampering wide-spread use of sub-

424   nano clusters in catalysis.

425   **Methods**

426   **Instrument design.** Past publications detailed the instrument design and protocols used

427   in this study[13,14,16]. Briefly, Pt_n^+ cluster ions were produced via laser ablation of a Pt target,

428   collected by a series of quadrupole ion guides, mass selected by a quadruple mass filter, and then

429   guided into the ultra-high vacuum system, where they were deposited on the catalyst support.

430   The support consisted of a thin alumina film grown on a Ta (110) single crystal, which was

431   mounted via heater wires to a cryostat allowing temperature control in the 120 K to 1000 K

432   range. For cleaning, the sample could be heated by electron bombardment; from behind the

433   cryostat, a filament allowed bombardment of electrons to the single crystal, that could heat the

434   crystal to over 2100 K. At that temperature, the alumina film and any deposited clusters desorb,

435   and the sample was found to be clean by X-ray photoelectron spectroscopy (XPS).

436 **Alumina film growth.** A fresh alumina film was grown on the clean Ta (110) single

437 crystal before each experiment, by evaporating Al in 5×10^{-6} Torr of O_2 at sample temperature of

438 970 K. These growth conditions produce alumina with a distorted hexagonal lattice that

439 resembles both γ-alumina (111) or α-alumina (0001) [26,27]. Film thickness was monitored by XPS

440 and was in the 4 to 6 nm range, which we previously found to give chemistry independent of

441 film thickness [28].

442 **Pt$_4$/alumina sample preparation.** Pt_n^+ clusters of the desired size, Pt_4 in this case, were

443 deposited on the alumina film with deposition energy of ~1 eV/atom and coverage equivalent to

444 ~0.1 monolayer (ML), corresponding to 1.5×10^{14} Pt atoms/cm^2. Just prior to deposition, the

445 sample was flashed to 750 K to desorb any adventitious adsorbates, and then cluster deposition

446 was carried out as the sample cooled, starting at 300 K.

447 **Pt$_4$Ge/alumina sample preparation.** The approach used to prepare alumina-supported

448 Pt_nGe_m clusters was similar to that used in previous studies of Pt_nSn_m/alumina and

449 Pt_nSn_m/SiO_2.[13,29] In essence, the Pt clusters were used as seeds to obtain selective, self-limiting

450 deposition by exposing the Pt$_4$/alumina sample to a 60 L dose of $GeCl_4$ vapor, then to 6000 L of

451 H_2. The $GeCl_4$ preferentially binds to the Pt_n clusters, and the number of molecules that bind

452 depends on the size of the cluster. When exposed to H_2, Cl reacts and desorbs as HCl, which can

453 be detected mass spectrometrically. The final stage in the preparation was to heat the samples to

454 750K to desorb any remaining Cl atoms (as HCl) as well as to remove excess H atoms. The

455 samples were characterized by X-ray photoelectron spectroscopy (XPS). The Pt_n clusters were

456 found to "seed" preferential Ge deposition on the clusters, resulting one Ge atom for every Pt_4

457 cluster deposited as discussed above. The non-specific Ge deposition at defects in the alumina

458 support film also occurs, but ethylene temperature programmed desorption, as shown above, of

459 the support-bound Ge atoms did not show evidence of any effects in the chemistry of ethylene

dehydrogenation. To assess that the coke suppressing effects of Pt_4Ge was not caused by the presence of Pt_4 clusters on the large amount of non-specific binding Ge on the alumina, 0.1 ML Pt_4 clusters were deposited onto the non-specific Ge dosed alumina surfaces (also 60 L of $GeCl_4$, then 6000 L of H_2 dosed) followed by C_2D_4 TPD, dehydrogenation of ethylene was still substantial and clear evidence of deactivation was observed with every TPD cycle, thus failing to prevent sintering and coke formation as shown in the supportive information (Fig. S12).

XPS quantification. The Ge $2p_{3/2}$ peak intensity for Pt_4Ge was larger than that of pure Ge, hence indicating Ge can be selective deposited on the surface of Pt_4 clusters. Samples were analyzed via Al Kα XPS and the raw intensities were corrected to account for the slight changes in spectrometer sensitivity and X-ray intensity using the Al 2s intensities from the alumina support (details in Supplementary Information).

Temperature programmed desorption (TPD) experimental procedures. TPD was used to investigate C_2D_4 desorption and dehydrogenation/carbon deposition chemistry on the samples. To start each TPD cycle, the samples was held at 150 K and exposed to a 10 L dose of C_2D_4, which is sufficient to saturate all binding sites that are stable at 150 K. The sample was then heated at 3 K *per* second to 750 K, while monitoring desorption of species of interest (principally C_2D_4 and D_2) using a differentially pumped mass spectrometer that views the sample through a 2.5 mm aperture on a skimmer cone, positioned ~0.5 mm from the sample surface. The relationship between numbers of molecules desorbing from the sample and numbers of ions detected by the mass spectrometer was determined using a procedure described elsewhere[13], calibrated by leaking C_2D_4 or D_2 into the main UHV chamber at measured pressures to create well defined fluxes of into the mass spectrometer.

Computational Methods. Global optimization of the Pt_4Ge/alumina structures was performed with plane-wave density functional theory (PW-DFT) using the Vienna Ab-initio

Simulation Package (VASP) [30-32] with projector augmented wave (PAW) potentials [33], using the

PBE functional [34]. The energy cutoff for the plane waves was chosen as 400.0 eV, and Gaussian

smearing with a sigma of 0.1 was used, while the electronic energy convergence parameter was

chosen as 10^{-6} eV. The D3 dispersion correction was used [35]. The model substrate used was an α-

alumina(0001) surface with cell parameters of a = 4.807 Å and c = 13.126 Å, previously found [20]

to best match the experimental support. The lower layers of the slab were kept fixed during

global optimization and subsequent adsorbate binding calculations. Only gamma-point sampling

was used due to the larger supercell used in the study.

Our initial Pt_4Ge structure geometries were obtained using our in-house code PGOPT [36],

which uses a bond-length distribution (BLDA) algorithm in order to generate structure that are

faster to optimize and less likely to result in errors during optimization. Once ~200 Pt_4Ge

structures had been generated, we took the thermally accessible structures within a cutoff of 0.4

eV, and generated a number of rough binding modes of C_2H_6, C_2H_4, and C_2H_2 using PGOPT,

which we later refined with VASP local optimizations to obtain the final binding modes. The

final ensemble of thermally-accessible catalyst states was computed for the initial cluster

structures, and re-computed for every intermediate on the reaction profile, by weighting the

optimized structures by the Boltzmann probability to be occupied at 700 K, based on DFT

electronic energies.

The Pt_4GeC_2 structures were generated from the thermally accessible acetylene binding

modes to Pt_4Ge by removing the hydrogens then optimizing the resulting structures with DFT.

Bader charge analysis [37-40] was performed to obtain the partial atomic charges. C-H activation

barriers for low-lying and important binding modes were calculated using the climbing-image

nudged elastic band (CI-NEB) method [39] and optimized until the force on all of the images was

less than 0.02 eV/Å. For ethylene and acetylene, multiple non-equivalent C-H bond breaking

508   events were attempted, focusing on the hydrogens closest to Pt atoms. For ethane, only the

509   elongated activated C-H bonds were broken.

510   DFT calculations on gas-phase models were performed with the Amsterdam Density

511   Functional (ADF) package, version 2019.304[41]. The PBE functional was used for all

512   calculations. Slater-type basis sets of triple-ζ + polarization quality were used on all atoms, with

513   orbitals up to 4d (Pt), 3d (Ge) and 1s (C) included in the frozen core[42].

514

515

516 **References and Notes**

517   1   Oliver-Meseguer, J., Cabrero-Antonino, J. R., Domínguez, I., Leyva-Pérez, A. & Corma, A. Small gold
518   clusters formed in solution give reaction turnover numbers of 107 at room temperature. *Science* **338**,
519   1452-1455 (2012).
520   2   Zandkarimi, B. & Alexandrova, A. N. Dynamics of Subnanometer Pt Clusters Can Break the Scaling
521   Relationships in Catalysis. *Journal of Physical Chemistry Letters* **10**, 460-467,
522   doi:10.1021/acs.jpclett.8b03680 (2019).
523   3   Joo, S. H. *et al.* Thermally stable Pt/mesoporous silica core–shell nanocatalysts for high-temperature
524   reactions. *Nature Materials* **8**, 126, doi:10.1038/nmat2329
525 https://www.nature.com/articles/nmat2329#supplementary-information (2008).
526   4   Bhasin, M., McCain, J., Vora, B., Imai, T. & Pujado, P. Dehydrogenation and oxydehydrogenation of
527   paraffins to olefins. *Applied Catalysis A: General* **221**, 397-419 (2001).
528   5   Nie, L., Meng, A., Yu, J. & Jaroniec, M. Hierarchically macro-mesoporous Pt/γ-Al 2 O 3 composite
529   microspheres for efficient formaldehyde oxidation at room temperature. *Scientific reports* **3**, 1-6
530   (2013).
531   6   Yang, D. *et al.* The preparation of hierarchical Pt/ZSM-5 catalysts and their performance for toluene
532   catalytic combustion. *Microporous and Mesoporous Materials* **296**, 109802 (2020).
533   7   Musselwhite, N., Na, K., Sabyrov, K., Alayoglu, S. & Somorjai, G. A. Mesoporous aluminosilicate catalysts
534   for the selective isomerization of n-Hexane: the roles of surface acidity and platinum metal. *Journal of*
535   *the American Chemical Society* **137**, 10231-10237 (2015).
536   8   Lu, J., Elam, J. W. & Stair, P. C. Synthesis and Stabilization of Supported Metal Catalysts by Atomic
537   Layer Deposition. *Acc. Chem. Res.* **46**, 1806-1815, doi:10.1021/ar300229c (2013).
538   9   Lu, J. L. *et al.* Coking- and Sintering-Resistant Palladium Catalysts Achieved Through Atomic Layer
539   Deposition. *Science* **335**, 1205-1208 (2012).
540   10   Gorey, T. J. *et al.* Selective Growth of Al_2O_3 on Size-selected Platinum Clusters by Atomic Layer
541   Deposition. *Surf. Sci.* **691**, 121485, doi:10.1016/j.susc.2019.121485 (2020).
542   11   Pham, H. N., Sattler, J. J., Weckhuysen, B. M. & Datye, A. K. Role of Sn in the Regeneration of Pt/γ-
543   Al_2O_3 Light Alkane Dehydrogenation Catalysts. *ACS Catal.* **6**, 2257-2264, doi:10.1021/acscatal.5b02917
544   (2016).
545   12   Iglesias-Juez, A. *et al.* A Combined in situ Time-resolved UV–Vis, Raman and High-energy Resolution
546   X-ray Absorption Spectroscopy Study on the Deactivation Behavior of Pt and PtSn Propane

547   Dehydrogenation Catalysts under Industrial Reaction Conditions. *J. Catal.* **276**, 268-279,
548   doi:10.1016/j.jcat.2010.09.018 (2010).

549   13   Li, G. *et al.* Sn-modification of Pt_7/Alumina Model Catalysts: Suppression of Carbon Deposition and
550   Enhanced Thermal Stability. *J. Chem. Phys.* **152**, 024702, doi:10.1063/1.5129686 (2020).

551   14   Gorey, T. J. *et al.* Coking-Resistant Sub-Nano Dehydrogenation Catalysts: Pt n Sn x/SiO2 (n= 4, 7).
552   *ACS Catalysis* **10**, 4543-4558 (2020).

553   15   Zandkarimi, B. *et al.* Alloying with Sn suppresses sintering of size-selected subnano Pt clusters on SiO2
554   with and without adsorbates. *Chemistry of Materials* **32**, 8595-8605 (2020).

555   16   Ha, M.-A., Baxter, E. T., Cass, A. C., L.Anderson, S. & Alexandrova, A. N. Boron Switch for Selectivity of
556   Catalytic Dehydrogenation on Size-Selected Pt Clusters on Al_2O_3. *J. Am. Chem. Soc.* **139**, 11568-11575,
557   doi:10.1021/jacs.7b05894 (2017).

558   17   Jimenez-Izal, E., Liu, J.-Y. & Alexandrova, A. Germanium as Key Dopant to Boost the Catalytic
559   Performance of Small Platinum Clusters for Alkane Dehydrogenation. *J. Catal.* **374**, 93-100,
560   doi:10.1016/j.jcat.2019.04.034 (2019).

561   18   Mariscal, R., Fierro, J. L., Yori, J. C., Parera, J. M. & Grau, J. M. Evolution of the properties of PtGe/Al2O3
562   reforming catalysts with Ge content. *Applied Catalysis A: General* **327**, 123-131 (2007).

563   19   Ballarini, A. D., de Miguel, S., Castro, A. & Scelza, O. n-decane dehydrogenation on bimetallic PtSn
564   and PtGe catalysts prepared by dip-coating. *Catalysis in Industry* **5**, 283-296,
565   doi:10.1134/S2070050413040028 (2013).

566   20   Baxter, E. T., Ha, M.-A., Alexandrova, A. & Anderson, S. L. Ethylene Dehydrogenation on $Pt_{4,7,8}$ Clusters
567   on Al_2O_3: Strong Cluster-Size Dependence Linked to Preferred Catalyst Morphologies. *ACS Catal.* **7**,
568   3322-3335, doi:10.1021/acscatal.7b00409 (2017).

569   21   Redhead, P. A. Thermal desorption of gases. *Vacuum* **12**, 203-211,
570   doi:http://dx.doi.org/10.1016/0042-207X(62)90978-8 (1962).

571   22   Yeh, J. J. & Lindau, I. Atomic Subshell Photoionization Cross Sections and Asymmetry Parameters: 1<
572   Z < 103. *Atomic Data and Nuclear Data Tables* **32**, 1-155 (1985).

573   23   Dai, Y. *et al.* Inherent Size Effects on XANES of Nanometer Metal Clusters: Size-Selected Platinum
574   Clusters on Silica. *J. Phys. Chem. C.* **121**, 361-374, doi:10.1021/acs.jpcc.6b10167 (2017).

575   24   Rodríguez, J. I. *et al.* A high performance grid-based algorithm for computing QTAIM properties.
576   *Chemical Physics Letters* **472**, 149-152 (2009).

577   25   Rodríguez, J. I. An efficient method for computing the QTAIM topology of a scalar field: The electron
578   density case. *Journal of computational chemistry* **34**, 681-686 (2013).

579   26   Madey, T. E. in *Chemisorption and Reactivity on Supported Clusters and Thin Films* Vol. 331 (eds
580   Richard M Lambert & Gianfranco Pacchioni) 105-116 (Kluwer Academic Publishers, 1997).

581   27   Chen, P. J. & Goodman, D. W. Epitaxial growth of ultrathin Al_2O_3 films on Ta(110). *Surf. Sci.* **312**, L767-
582   L773 (1994).

583   28   Kane, M. D., Roberts, F. S. & Anderson, S. L. Effects of Alumina Thickness on CO Oxidation Activity over
584   Pd_{20}/Alumina/Re(0001): Correlated Effects of Alumina Electronic Properties and Pd_{20} Geometry on
585   Activity. *J. Phys. Chem. C.* **119**, 1359–1375, doi:10.1021/jp5093543 (2015).

586   29   Gorey, T. J. *et al.* Preparation of Size and Composition Controlled Pt_nSn_x/SiO2 (n = 4, 7, 24) Bimetallic
587   Model Catalysts with Atomic Layer Deposition. *J. Phys. Chem. C.* **123**, 16194-16209,
588   doi:10.1021/acs.jpcc.9b02745 (2019).

589   30   Kresse, G. & Hafner, J. Ab initio Molecular Dynamics for Liquid Metals. *Phys. Rev. B* **47**, 558,
590   doi:10.1103/physrevb.47.558 (1993).

591   31   Kresse, G. & Furthmüller, J. Efficient Iterative Schemes for ab initio Total-energy Calculations using a
592   Plane-wave Basis Set. *Phys. Rev. B* **54**, 11169, doi:10.1103/PhysRevB.54.11169 (1996).

593   32   Kresse, G. & Furthmüller, J. Efficiency of ab-initio Total Energy Calculations for Metals and
594   Semiconductors using a Plane-wave Basis Set. *Comput. Mater. Sci.* **6**, 15-50, doi:10.1016/0927-

595   0256(96)00008-0 (1996).
596 33 Kresse, G. & Joubert, D. From Ultrasoft Pseudopotentials to the Projector Augmented-wave Method.
597   *Phys. Rev. B.* **59**, 1758-1775, doi:10.1103/PhysRevB.59.1758 (1999).
598 34 Perdew, J. P., Burke, K. & Ernzerhof, M. Generalized Gradient Approximation Made Simple. *Phys. Rev.*
599   *Lett.* **77**, 3865, doi:10.1103/PhysRevLett.77.3865 (1996).
600 35 Grimme, S., Antony, J., Ehrlich, S. & Krieg, H. A consistent and accurate ab initio parametrization of
601   density functional dispersion correction (DFT-D) for the 94 elements H-Pu. *The Journal of Chemical*
602   *Physics* **132**, 154104, doi:10.1063/1.3382344 (2010).
603 36 Zhai, H. & Alexandrova, A. N. Ensemble-Average Representation of Pt Clusters in Conditions of
604   Catalysis Accessed through GPU Accelerated Deep Neural Network Fitting Global Optimization. *J.*
605   *Chem. Theory Comput.* **12**, 6213-6226, doi:10.1021/acs.jctc.6b00994 (2016).
606 37 Tang, W., Sanville, E. & Henkelman, G. A Grid-based Bader Analysis Algorithm without Lattice Bias. *J.*
607   *Condens. Matter. Phys.* **21**, 084204, doi:10.1088/0953-8984/21/8/084204 (2009).
608 38 Sanville, E., Kenny, S. D., Smith, R. & Henkelman, G. Improved Grid-based Algorithm for Bader Charge
609   Allocation. *J. Comput. Chem.* **28**, 899-908, doi:10.1002/jcc.20575 (2007).
610 39 Henkelman, G., Uberuaga, B. P. & Jónsson, H. A Climbing Image Nudged Elastic Band Method for
611   Finding Saddle Points and Minimum Energy Paths. *J. Chem. Phys.* **113**, 9901-9904,
612   doi:10.1063/1.1329672 (2000).
613 40 Yu, M. & Trinkle, D. R. Accurate and Efficient Algorithm for Bader Charge Integration. *J. Chem. Phys.*
614   **134**, 064111, doi:10.1063/1.3553716 (2011).
615 41 Te Velde, G. t. *et al.* Chemistry with ADF. *Journal of Computational Chemistry* **22**, 931-967 (2001).
616 42 Van Lenthe, E. & Baerends, E. J. Optimized Slater-type basis sets for the elements 1–118. *Journal of*
617   *computational chemistry* **24**, 1142-1156 (2003).
618

Acknowledgments

Author Contributions

ANA and SLA conceived and supervised the research, reviewed and edited the paper. GL and PP wrote the original draft and developed the methodology. GL performed the experimental work. PP conducted all DFT calculations. TM assisted in obtaining the initial experimental conditions and conducted TEM experiments.

Competing interests

Authors declare that they have no competing interests.

630   **Additional information**

631   **Supplementary Information**

632   **Data availability** Data behind all Figs. in the paper will be uploaded to a publically available

633   archive with link provided at time of publication.

634   **Correspondence and requests for materials** should be addressed to Anastassia N. Alexandrova
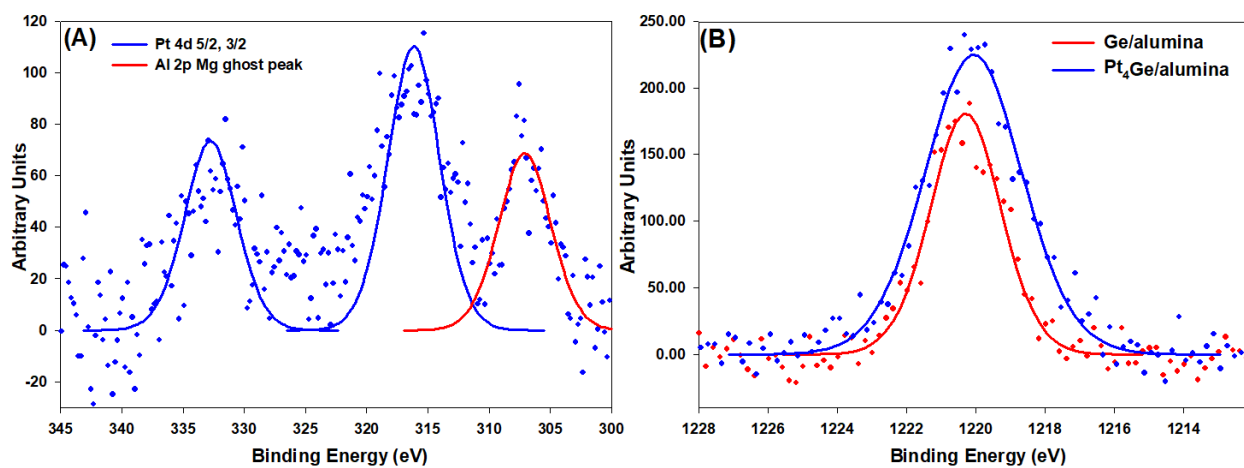
635   and Scott L. Anderson.

Fig. 1 XPS showing selective binding of Ge to Pt clusters. (A) XPS of Pt 4d 5/2 and 3/2 of Pt$_4$Ge/alumina, red colored peak is from Mg contamination in the Al source. **(B)** Ge 2p 3/2 peak for Ge/alumina in red and Pt$_4$Ge/alumina in blue.
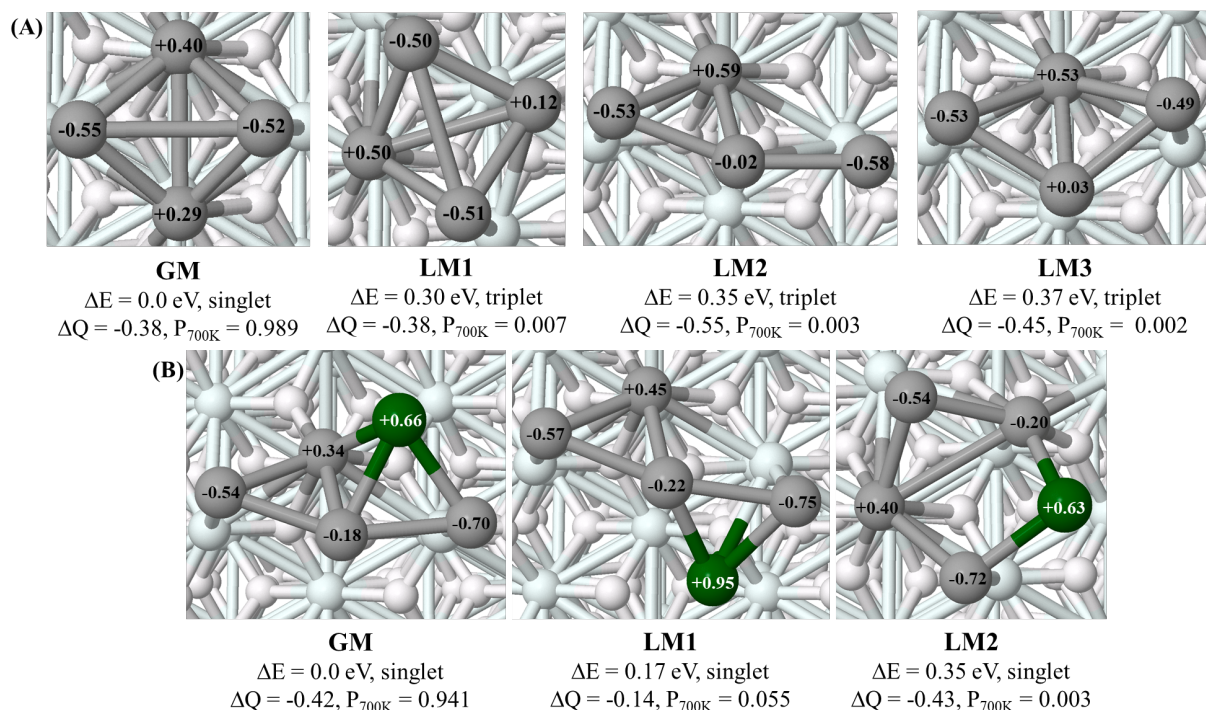
Fig. 2 Thermally accessible structures, which are within 0.4 eV of the lowest energy structure. (**A**) Computed thermally accessible structures of Pt$_4$/alumina. (**B**) Computed thermally accessible structures of Pt$_4$Ge/alumina. The spin state, net support-to-cluster electron transfer (ΔQ), Bader charges on each cluster atom, and the thermal population at 700 K (P_{700K}) are shown. GM = global minimum. For each local minimum (LM), the energy above the GM (ΔE) is given.
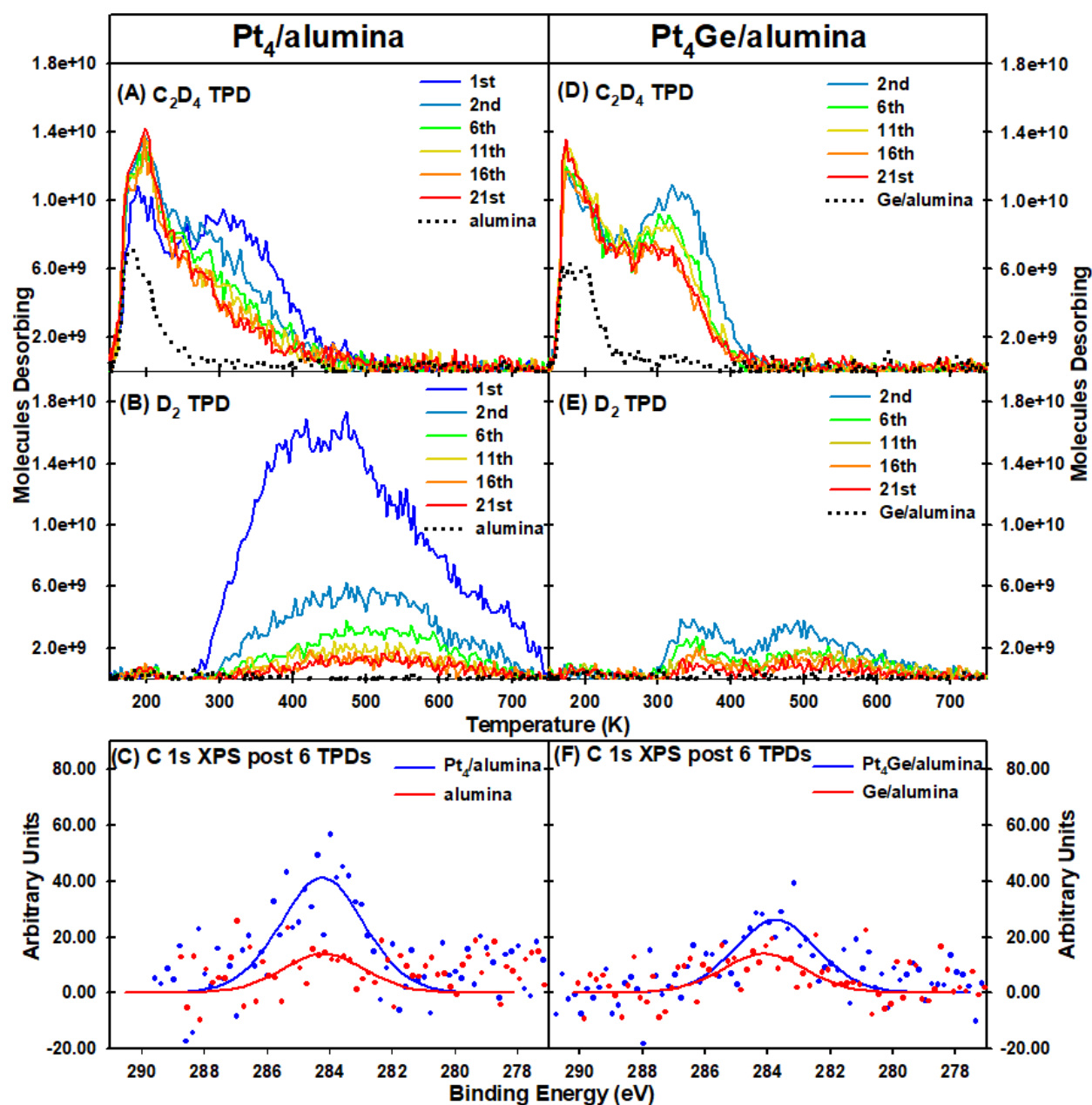
Fig. 3 Temperature Programmed Desorption (TPD) results showing C$_2$D$_4$ and D$_2$ desorption; with Xray photoelectron spectroscopy (XPS) scans of the C 1s region. Left column: Pt$_4$/alumina. Right column: Pt$_4$Ge/alumina. (**A**) and (**D**) show desorption of intact C$_2$D$_4$. (**B**) and (**E**) show desorption of D$_2$. (**C**) and (**F**) show carbon 1s XPS from Pt$_4$/alumina and Pt$_4$Ge/alumina after 6 TPD cycles, control samples (alumina and Ge/alumina) were also probed post 6 TPDs.
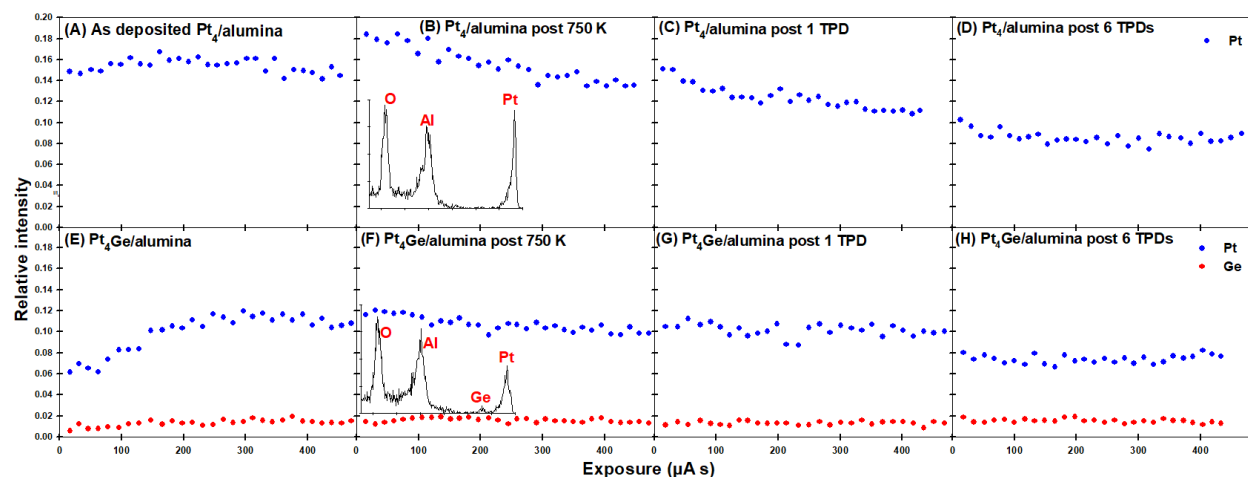
Fig. 4 Low energy He$^+$ ion scattering spectroscopy (ISS) showing relative intensities of Pt and Ge. (A) as deposited Pt$_4$/alumina, (B) Pt$_4$/alumina post 750 K heat, inset shows the raw ISS at ~ 30 μAs exposure. (C) Pt$_4$/alumina post 1 C$_2$D$_4$ TPD, (D) Pt$_4$/alumina post 6 C$_2$D$_4$ TPDs, (E) As-prepared Pt$_4$Ge/alumina, (F) Pt$_4$Ge/alumina post 750 K heat, inset shows the raw ISS at ~ 30 μAs exposure. (G) Pt$_4$Ge/alumina post 1 C$_2$D$_4$ TPD and (H) Pt$_4$Ge/alumina post 6 C$_2$D$_4$ TPDs.
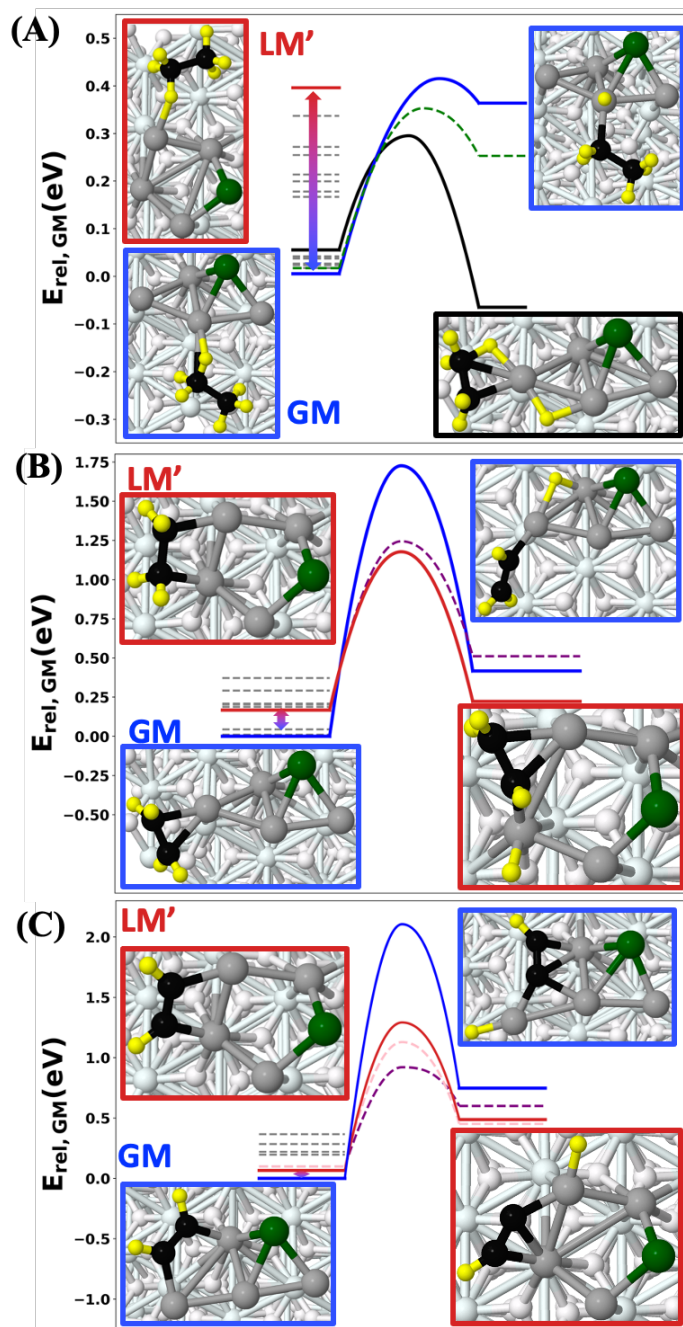
Fig. 5 Representative ethane, ethylene, and acetylene C-H activation barriers for Pt₄Ge. C-H activation barriers on Pt₄Ge/alumina thermal ensemble of states for (a) ethane (b) ethylene and (c) acetylene.
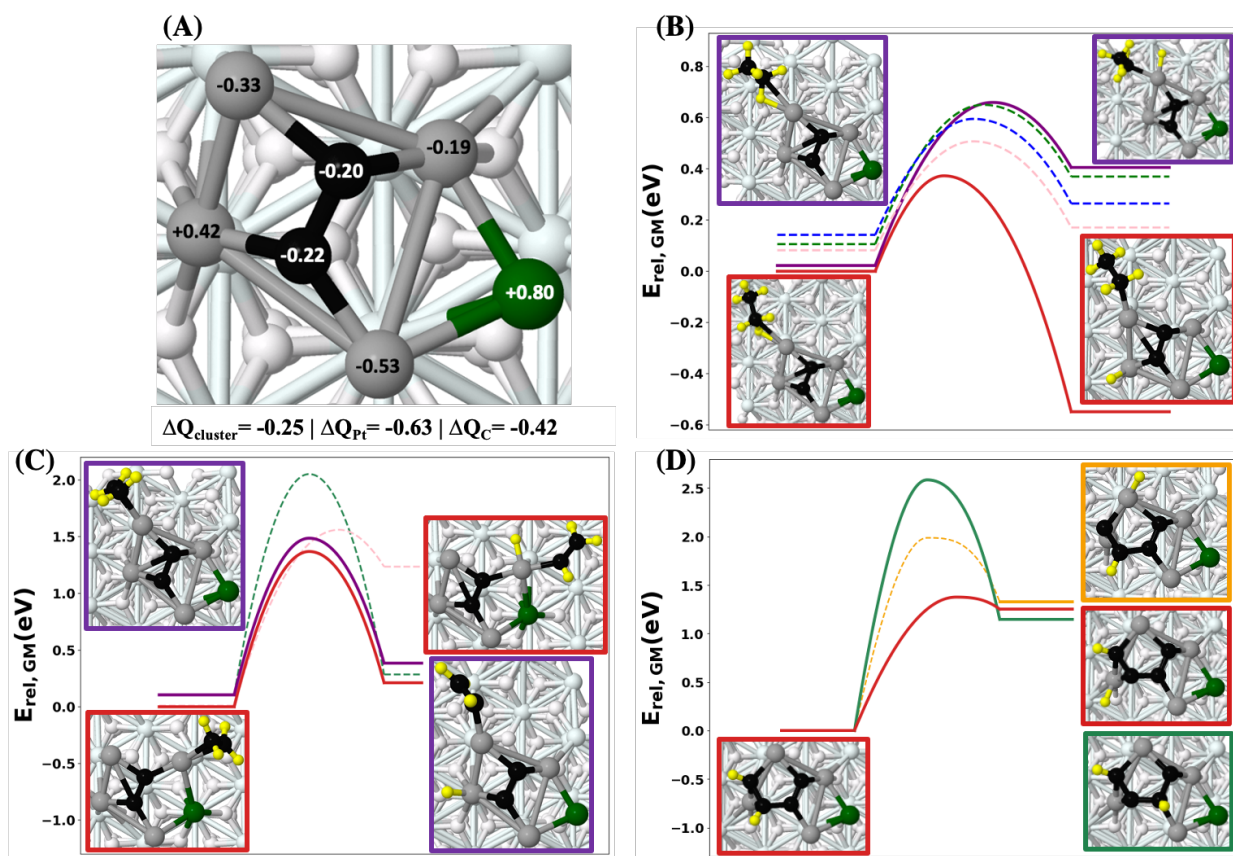
(A) ΔQ_cluster = -0.25 | ΔQ_Pt = -0.63 | ΔQ_C = -0.42

Fig. 6 Representative ethane, ethylene, and acetylene C-H activation barriers on Pt₄GeC₂,

the steady-state catalyst. (a) the one thermally accessible Pt_4GeC_2 isomer, and (b)

representative C-H activation barriers for ethane, (c) ethylene, and (d) acetylene, with certain key

structures inset.